IEEE Access
Multidisciplinary | Rapid Review | Open Access Journal

Received March 12, 2020, accepted March 26, 2020, date of publication April 6, 2020, date of current version May 8, 2020.

Digital Object Identifier 10.1109/ACCESS.2020.2986082

Sporadic-Slot Photonic-Crystal Waveguide for All-Optical Buffers With Low-Dispersion, Distortion, and Insertion Loss

SAYED ELSHAHAT[1,2,3,4], ISRAA ABOOD[3], ZIXIAN LIANG[1], JIHONG PEI[2], (Member, IEEE), AND ZHENGBIAO OUYANG[3], (Member, IEEE)

[1]Institute of Microscale Optoelectronics, Shenzhen University, Shenzhen 518060, China
[2]College of Electronics and Information Technology, Shenzhen University, Shenzhen 518060, China
[3]College of Physics and Optoelectronics Engineering, Shenzhen University, Shenzhen 518060, China
[4]Department of Physics, Faculty of Science, Assiut University, Assiut 71516, Egypt

Corresponding author: Zhengbiao Ouyang (zbouyang@szu.edu.cn)

This work was supported in part by the National Natural Science Foundation of China under Grant 61275043, Grant 61307048, Grant 60877034, and Grant 61605128, in part by the GDNSF under Grant 2020A1515011154, and in part by the SZSF under Grant JCYJ20190808151017218, 20180123.

ABSTRACT A novel structure is studied with implanting sporadic slots inside a photonic crystal waveguide (PCW) to form sporadic-slot PCW (SSPCW) for realizing compact, all-optical buffers with low-dispersion, distortion, and attenuation (DDA). We implement the first demonstration that, to the best of our knowledge, the SSPCW works for both TE- and TM-modes all-optical buffers and slow-light waveguides. High buffer performance and wider transmission bandwidth in telecommunication band are obtained, which are guaranteed through bit rate optimization that exceeded 2 Tb/s for both TE and TM modes in ultra-low dispersion region which is 20 times greater than that required for 5G mobile communications and it is also useful for all-optical signal processing. The storage length of 1 bit is obtained as 4.5202 μm for TE mode and 6.0525 μm for TM mode. Moreover, a low relative pulse distortion of 0.0801% μm^{-1} along the propagation path per unit length is acquired for a 0.63 ps pulse. Besides, the attenuation coefficient of the optical power pulse between the input and output is 0.0170 dB/μm. Additionally, the deigned SSPCW is insensitive for small variations of waveguide parameters and the deviation is virtually negligible between the simulated results and that of the fabricated structures with totally acceptable tolerance below $\pm$3 nm, which is the challenge in the fabrication process of conventional PCW and PCW-cavity.

INDEX TERMS Sporadic-slots, photonic crystal waveguide, dispersion, distortion, attenuation.

I. INTRODUCTION

Photonic crystals (PhCs) have been scrutinized for miscellaneous applications, as a highly successful and unique platform for manipulating light in microscopic dimensions and designing their dispersions for particular needs [1]. PhCs have the potential in realizing optical processors to meet the need for higher CPU speeds. The common key for all-optical processors is the optical buffer, which stores the optical packets temporarily and fine-tunes CPU timing. Slow-light property in PhC waveguide (PCW) provides the basis for efficient buffering of optical packets in flexible on-chip optical signal processing [2]. Moreover, they can operate at room temperature with wide bandwidths [3] and possess low dispersion and distortion for light propagation [4]. With technologically valuable developmentsof silicon-based PCWs, slotted photonic crystal waveguide (SPCW)attracted the attention of many researchersdue to the combination of two important features in numerous applications: it can merge the abilities to confine light in the low-index material in slots and enhancing the slow-light property of PCWs [5]. In PCWs, the optical confinements are due to the deeper spreading of optical mode profile inside the PhC lattice with reducing group velocity [6], and generally the propagation loss upsurges for the slow-light modes. Further, some of the benefits derived from the slow-light effect can be debilitated. Contrariwise, in the SPCW due to the high index contrast of the silicon platform, the optical confinement consolidates

The associate editor coordinating the review of this manuscript and approving it for publication was Nagendra Prasad Pathak.

This work is licensed under a Creative Commons Attribution 4.0 License. For more information, see https://creativecommons.org/licenses/by/4.0/

with the reduction of group velocity. At the interface with the high contrast of index, the guided modes are required to be highly intensive in the low index region (slots). Accordingly, the concentration percentage of energy in this region will increase instead of decrease by approaching the photonic bandgap edge [7]. This advantage can be utilized in applications mainly for compact optical communications [8], various types of sensor devices [9], [10] and probable applications in 5G communication systems.

Recently, sundry SPCW structures proposed for realizing slow-light property [4], [11], [12] have been designed based on two main frameworks: changing the periodic arrays or/and shape of the scatters. Examples of changing the periodic arrays of scatters are, adjusting the size of the hole [13], fine-tuning the holes' positions adjacent to the slot position [14], and changing the slot size [15], [16]. It turned out that it was difficult to precisely control the size of holes for a photonic lattice and reproduction in the fabrication processes [1]. Examples of changing the shape of the scatters are, ring-shaped [17], ellipse-shaped [11], eye-shaped [18], and crescent-shaped designs [19]. Nevertheless, novel structures are to be inspected based on square photonic crystal slab with a large and fixed size of all air holes together with SSPCW for realizing compact, all-optical buffers with low dispersion, distortion, and attenuation (DDA). In this paper, we proposed a unique platform from SSPCW for both TE- and TM-modes of all-optical buffers and slow-light waveguides. High buffer performance and ultra-wider transmission bandwidth in the telecommunication band are obtained.

II. GENERAL EQUATIONS OF SLOW LIGHT AND OPTICAL BUFFERS

To investigate and heighten slow-light properties, some formulae and definitions are requisite to be explained. The slow-light properties can be evaluated by the group index n_g, which is defined as the ratio of light speed in vacuum c to group velocity v_g, so [18]

$$n_g = \frac{c}{v_g} = \frac{dK}{dU} \tag{1}$$

where $U = \omega a/2\pi c = a/\lambda$ and $K = ka/2\pi$ are the normalized frequency and normalized wave vector, respectively. Considering the refraction effect of material to light, the group velocity v_g of the guided modes is defined as the derived number of angular frequency ω to wave vector k, i.e., $v_g = d\omega/dk$. According to Eq. (1), the slop of a dispersion curve or the first derivative of dispersion relation between U and K vector is n_g. Furthermore, for all-inclusive valuation of slow-light property, normalized-delay-bandwidth-product (*NDBP*) is more frequently considered for devices at different operating frequencies and/or different lengths. *NDBP* is defined as:

$$NDBP = \bar{n}_g \times \frac{\Delta U}{U_0} \tag{2}$$

where U_0 is the normalized central frequency of the linear slope region over normalized bandwidth ΔU of a linear region within $\pm 7.5\%$ of n_g variation about $\bar{n}_g$. To avoid optical signal distortion, ΔU should be inside the linear region. Moreover, for ultra-low dispersion U_0 should be in the flattest dispersion curve and region. For all calculations in this study, n_g variation is less than all other reported previously which restricted by $\pm 10\%$ [20]. The $\pm 7.5\%$ variation of the group index is a sufficient guarantor to achieve ultra-low dispersion below 5×10^4 $(a/2\pi c^2)$.

Alongside the transmission function of data connection, the SSPCW is superior for comprehending all-optical buffers in practical applications for its compact physical size in addition to its admirable performance of data transmission through slow-light modes. Consequently, the number of parameters to characterize the full buffering performance should be mentioned. The entering data to the buffer (slow-light region) contains a sequence of packets (i.e., a series of bits) with an optical central wavelength λ_0. Each packet has a data bit period of τ_{bit} with a base-bandwidth $B_{packet} = 1/\tau_{bit}$. The optical data bandwidth in rad/s is $\Delta\dot{\omega} = 4\pi B_{packet}$ [21], which links with the normalized bandwidth by $\Delta U = (a/2\pi c)\Delta\dot{\omega}$. The first key figure of merit (FOM) for buffering is the bit rate R_b which is well-defined by the number of bits per second. From the view of bit flow in a return-to-zero (RZ) format, R_b can be calculated by [22]:

$$R_b = \frac{B_{Packet}}{2} = \frac{c \times \Delta U}{4a} \tag{3}$$

For the constant value of lattice constant a, R_b has a direct dependence on the bandwidth. The second key FOM parameter is the storage time T_s for the buffers in the slow-light region of length L, calculated by

$$T_s = \frac{L}{\bar{v}_g} = \frac{L}{c} \times \bar{n}_g \tag{4}$$

Equation (4) shows that high $\bar{n}_g$ is required for delay-time enhancement, which, however, leads to the reduction of bandwidth or the bit rate, and vice versa. The third key FOM parameter is the storage capacity (delay-bandwidth-product) C, which is defined by the maximum number of stored bits in the buffer. From Eqs. (3) and (4), C can be written as:

$$C = T_s \times B_{Packet} = \frac{L}{2a} \times (\bar{n}_g \Delta U) \tag{5}$$

It's obvious from Eq. 5 that C is directly proportional to the product of $\bar{n}_g$ and ΔU. The fourth key FOM parameter for all delay-line buffering is the minimum physical size of each stored bit in the buffer L_{bit}, and by noticing Eq. (5) L_{bit} can be written as: [21]

$$L_{bit} = \bar{v}_g \times \tau_{bit} = \frac{2a}{(\bar{n}_g \Delta U)} \tag{6}$$

which is eventually limited by the maximum storage density (*SD*, the fifth key FOM parameter) of data bits in the buffer [23]. *SD* is defined as the number of stored bits per unit length, and from Eq. (6) *SD* can be written as:

$$SD = \frac{1}{L_{bit}} = \frac{C}{L} = \frac{(\bar{n}_g \Delta U)}{2a} \tag{7}$$

Subsequently, the guarantee for high capability all-optical buffering and slow light is the high compatible value between $\overline{n}_g$ and ΔU, hence the product of $\overline{n}_g$ and ΔU is the duty-bound quantity to be optimized. In real applications, for a fixed delay line of length L, the recommended structure has to be considered in line with the request of the delay time, bit length and storage density.

III. PHYSICAL MODEL AND SIMULATION RESULTS

The inspected structure is based on a square photonic crystal slab of $n = 3.48$ in silicon-on-insulator substrate (SOI) with large, fixed-size air holes of radius $r = 0.44a$, where a is the lattice constant. The proposed SSPCW of W2 PCW is constructed by switching the central two lines of air holes with one line of sporadic slots. Each slot has a width w_x and length l_z, and the shifting between every two sequentialslots in the Z direction is s_z as shown in Fig. 1. For the minimization of scattering loss in the propagation direction, the lattice constant is kept as a constant between every two sequential slots to ensure optical-phase-matching between adjacent unit cells [24]. By appropriately modifying the sporadic slot dimensions, high buffer performance and wider transmission bandwidth are investigated. In the subsequent process, firstly, photonic band gaps (PBGs) were calculated for transverse electric/magnetic modes (TE/TM) by the spectral features of the basic square PhC structure for silicon slab of $n = 3.48$ and air holes of radius $r = 0.44a$. The output in time domain is transformed into the frequency domain through Fast-Fourier-Transform (FFT) algorithm. Figure 2 shows the transmission spectrum of the basic PhC along the propagation direction Γ–X. Suppose, for instance, that the dielectric constant is independent on the Y-axis. Then the solutions all take the form of either TE modes with nonzero (H_x, H_z, E_y) or TM modes with nonzero (H_y, E_x, E_z). In all-purpose, conventional PhC structures are: either, slab on insulator substrate arranged by a triangular lattice of air holes supporting TM polarized mode, or square-lattice from dielectric rods arranged in air background supporting TE polarized mode.

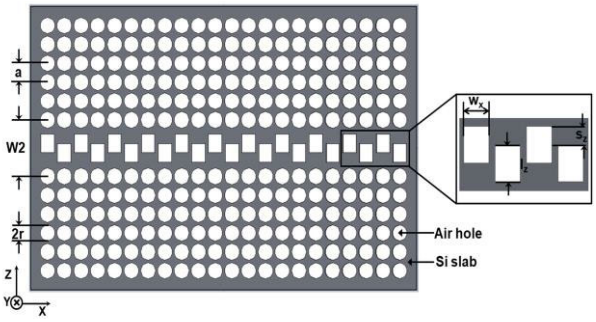

FIGURE 1. Schematic diagram of the paradigm SSPCW geometry.

Fortunately, the square photonic crystal slab of $n = 3.48$ with large and fixed size of all air holes can supporting TE and TM polarized modes in our proposed case as shown in Fig. 2. Transmission spectrum has one TE-PBG of

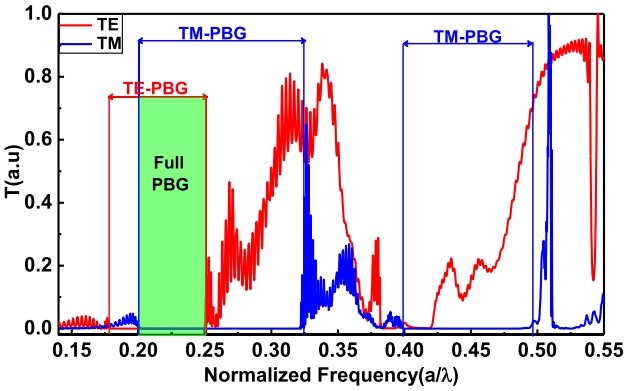

FIGURE 2. Transmission spectra of the basic PhC slab with $n = 3.48$ and air-hole radius $r = 0.44a$.

normalized frequency from $\omega a/2\pi c = 0.1775$ to 0.2517, and two large TM-PBGs of normalized frequencies from $\omega a/2\pi c = 0.2015$ to 0.3224 and from $\omega a/2\pi c = 0.3985$ to 0.4967. For all-purpose extent, high bit rate and a low DDA can be acquired via optimization of the structure parameters (e.g., changing the radius, position, shape and refractive index and so on [4], [25]–[27]). However, in this paper, we introduce a unique method for both TE/TM polarized modes to get ultra-high bit rate and ultra-low DDA.

We first consider the linear slot with slot width $w_x = 1.0a$ and the shifting $s_z = 0.0a$ but with different slot length l_z. This corresponds to a straight air slot in the center of the structure.

The dispersion curves in Fig. 3(a) are elaborated by plane-wave-expansion (PWE) method using the BandSOLVE module of software Rsoft for the SSPCW with $w_x = 1.0a$, $s_z = 0.0a$, and l_z varying from $0.55a$ to $0.65a$. It supports TE and TM modes as shown in Fig. 2(a). Moreover, as shown from the inset of Fig. 2, the supercell periodic is selected for eigenmode calculations with a lateral length of two rows of air holes in the x-direction and eleven rows in the z-direction. It is large enough that the coupling among adjacent parallel waveguides, which are created due to the super-cell model, can be ignored. Furthermore, high resolutions are used for both x and z directions with 65536 plane waves which equal to the spatial grid points (64×256) in the calculations. The dash-dot line signifies the light line. Figure 3(b) shows the contour map of group velocity v_g/c for both TE and TM modes with l_z varying from $0.55a$ to $0.65a$ via normalized wavevector K. For TE mode, we can see perceptibly that the linearity for constant slope in the long K range decreases with increasing l_z and the smallest linearity of K range is around $l_z = 0.60a$, for which we concern on the area below the light line. For the realization of slow-wave devices, the dispersion curves of waveguide modes should be under the light line, because the modes located above the light line are extremely lossy and the modes below the light line are intrinsically lossless [26]. Interestingly, TM modes have an acceptable wideband at $l_z = 0.60a$. To make the simulation data in Fig.3 visible, we transferred it into Table 1. As is

TABLE 1. Slow-light and all-optical buffer parameters for different l_z at $w_x = 1.0a$ and $s_z = 0.0a$.

mode	l_z/a	ΔU	U_0	a(nm)	$\Delta\lambda$ at 1550 nm	$\overline{n}_g$	$NDBP$	T_s(ps)	R_b(Tb/s)	L_{bit}(μm)	SD(b/μm)
TE	0.55	0.0071	0.244	0.3783	44.78	13.63	0.3937	45.43	1.3978	7.873	0.1270
	0.575	0.0069	0.247	0.3824	43.07	14.03	0.3898	46.77	1.3445	7.952	0.1258
	0.60	0.0064	0.25	0.3881	39.44	14.30	0.3638	47.67	1.2311	8.520	0.1174
	0.625	0.0074	0.253	0.3915	45.33	15.20	0.4445	50.67	1.4150	6.974	0.1434
	0.65	0.0074	0.256	0.3971	44.74	15.30	0.3937	45.43	1.3967	7.019	0.1425
TM	0.55	0.0059	0.303	0.4694	30.18	11.69	0.2276	38.97	0.9423	13.62	0.0734
	0.575	0.0058	0.309	0.4783	28.93	12.20	0.2277	40.67	0.9032	13.61	0.0735
	0.60	0.0063	0.318	0.4925	30.97	11.82	0.2362	39.4	0.9669	13.12	0.0762
	0.625	0.0056	0.323	0.5013	26.82	11.60	0.2007	38.67	0.8373	15.44	0.0647
	0.65	0.0011	0.329	0.5096	5.089	42.00	0.1379	38.97	0.1589	22.48	0.0445

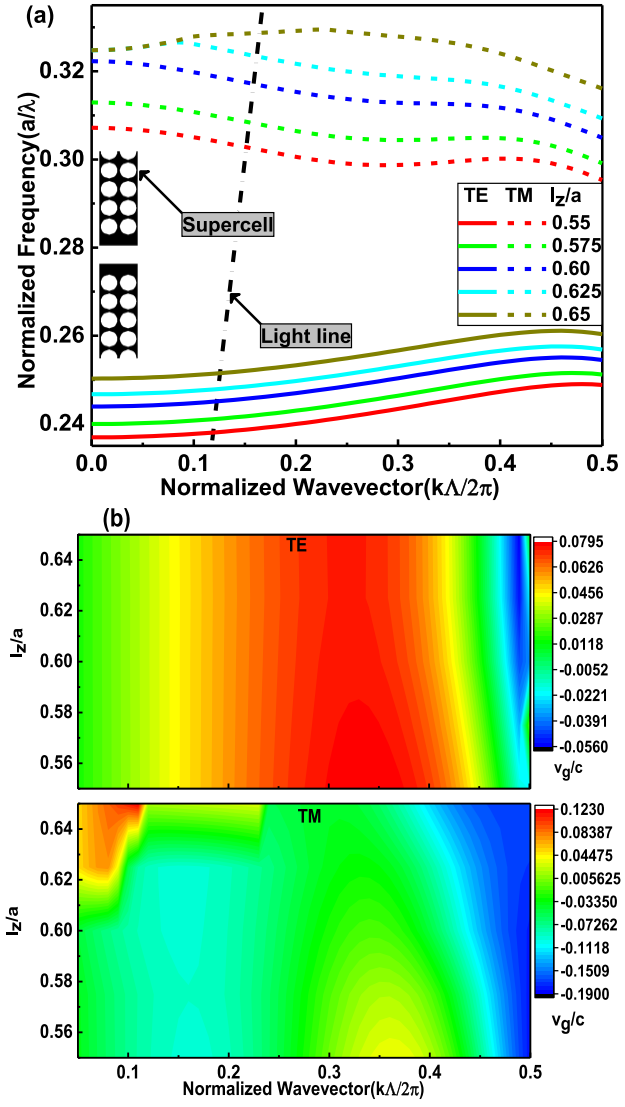

FIGURE 3. (a) Dispersion diagram of SSPCW at $w_x = 1.0a$ and $s_z = 0.0a$ for TE/TM modes with l_z varying from $0.55a$ to $0.65a$, where the inset shows the supercell for simulation; (b) contour map for TE/TM modes of group velocity v_g/c versus l_z and K.

known, the PWE method considers infinite-area structures, however, the calculations are good for practical applications when the structure length is much longer than the operating wavelength which has the order of the lattice constant. In our simulations, the delay line length L is taken as 1 mm, which is much longer than the wavelength, so our calculations are applicable [4], [22].

From Table 1, in the case of a straight-line slot with $w_x = 1.0a$, the optimum slot length is $l_z = 0.625a$ and $0.60a$ for TE and TM modes, respectively. These bit rates do not exceed 1.5 Tb/s and 1.0 Tb/s for TE and TM modes, respectively. The central wavelength can be scaled to be the optical communication wavelength of 1.55 μm by reducing the lattice constant a from 1 μm according to Table 1. Therefore, in this case to storage 1 bit, we need 6.9743 μm for TE (SD = 1 bit/6.9743 μm = 0.1434 bit/μm) and 13.1249 μm for TM (SD = 0.0762 bit/μm). It is not so satisfied as yet for applications, particularly for all-optical signal processing and new-generation communication systems in which high bit rates are needed with a small physical size of each bit which requires higher storage density. In the following, we will see that the SSPCW is the potential candidate for all-optical signal processing requirements. Our idea is physically based on the following: the sporadic slots in the proposed SSPCW act as microcavities of low index material (air slot). Meanwhile, each slot represents a defect and each defect can be considered as a cavity. Consequently, a series of slot cavities can be coupled together to form a line of defect cavities as a waveguide. The zigzag-arranged cavities provide more delay to the waves. The operating transmission bandwidth is enlarged based on the concept of impedance matching [26]. With the suitable design (suitable w_x and l_z values) and impedance matching, the transmission bandwidth can be wider on account of the group index.

In the following, $w_x \neq 1$ and will be varied from $0.85a$ to $0.95a$ with an increment of $\Delta w_x = 0.05a$, and the length l_z will be varied from $0.50a$ to $0.70a$ with an increment of $\Delta l_z = 0.025a$. In this case, the central region is a channel with a broken straight slot, i.e., having periodic air slots arranged in a silicon background. Fig. 4 shows the effect of changing w_x and l_z on the group velocity and normalized frequency. The inset of Fig. 4(a) shows the supercell for PWE calculations. For TE at $w_x = 0.85a$ and l_z changing from $0.50a$ to $0.70a$, it can be seen that most flat-band areas are located above the light line which has high losses and the ellipse-marked regions around $K = 0.4$ are the only small flat area for slow-light modes. Whereas, for $w_x = 0.90a$ and $0.95a$, linear dispersion regions in the long K range are

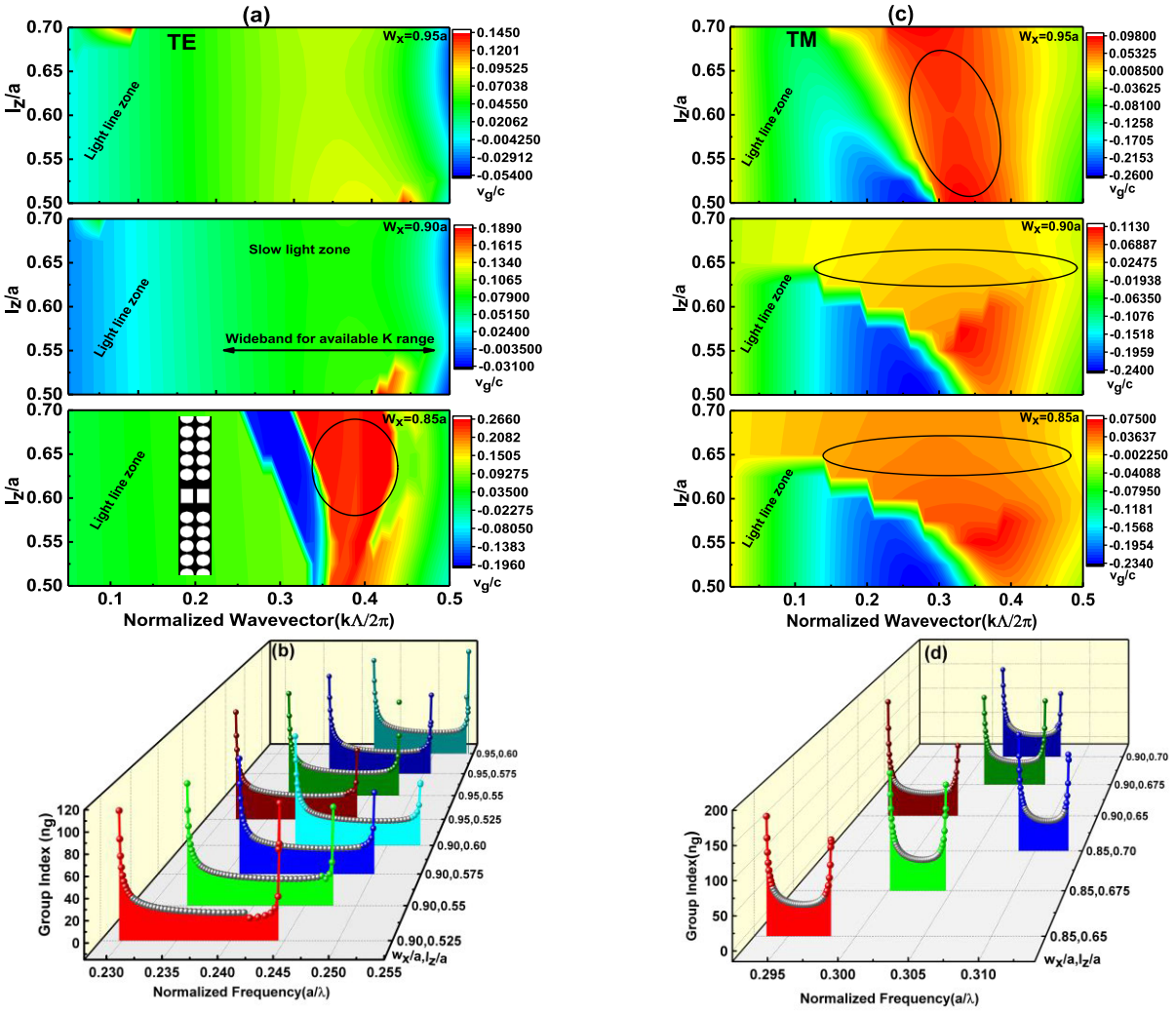

FIGURE 4. Group velocity v_g/c versus K, w_X and l_Z at $s_Z = 0.0a$ for (a) TE and (c) TM modes; n_g versus normalized frequency a/λ, w_X and l_Z for (b) TE and (d) TM modes.

available below the light line with wide bandwidth around $l_z = 0.55a$ as shown in Fig. 4(a). Moreover, for observing more clearly the transmission bandwidth, Fig. 4(b) shows the variation of n_g with normalized frequency for TE mode as l_z changing from $0.525a$ to $0.60a$ with $w_x = 0.90a$ and 0.95a. For TM mode at $w_x = 0.95a$ and l_z changing from $0.50a$ to $0.70a$, it's clear that the flat-band area located below the light line is small, as shown from the vertical ellipse-marked region around $K = 0.4$. Whereas for $w_x = 0.85a$ and $0.90a$, linear-dispersion regions in the long K range are available below the light line with wide bandwidth above $l_z = 0.625a$ as shown in Fig. 4(c). Moreover, for more clear observation of the transmission bandwidth, Fig. 4(d) shows the variation of n_g with normalized frequency for TM modes as l_z changing from $0.60a$ to $0.70a$ with $w_x = 0.85a$ and $0.90a$. The operating frequency bands within ± 7.5 % variation of n_g are colored by dark gray solid balls in Figs. 4(b, d). To compare the simulation results of Figs. 4(b, d) clearly, we transferred them into Table 2.

Table 2 shows the slow-light and all-optical buffer parameters at $w_x = 0.90a$, $0.95a$ combined with l_z changing from $0.525a$ to $0.60a$ by an increment of $\Delta l_z = 0.025a$ with $s_z = 0.0a$ for TE modes. Whereas for TM modes, l_z changes from $0.65a$ to $0.70a$ by an increment of $\Delta l_z = 0.025a$ combined with $w_x = 0.85a$, $0.90a$. The lattice constant a is ranged for the operating wavelength in the optical communication band around 1550 nm. Meanwhile, for TE modes, at $w_x = 0.90a$ and $l_z = 0.55a$ lead to the highest compatible value of $NDBP = 0.6858$ for the operating bandwidth and group index. By varying w_x and l_z, R_b exceeds 2 Tb/s in the ultra-low dispersion region which is 20 times the speed demonstrated for all-optical signal processing and 200 times the speed of 5G mobile communication, and it can also be used for 6G mobile communication network due to its high bit rate with the smallest physical size of each stored bit around 4.5202 μm. Furthermore, to store 1 bit, a space of 4.5202 μm length is needed, so the storage density SD is 0.2212 bit/μm. For TM modes, $w_x = 0.90a$ and $l_z = 0.65a$ lead to the

TABLE 2. Slow-light and all-optical buffer parameters under different values of w_x and l_z with $s_z = 0.0a$ for TE/TM.

Mode	w_x/a	l_z/a	ΔU	U_0	a(nm)	$\Delta\lambda$ at 1550 nm	$\overline{n}_g$	$NDBP$	T_s(ps)	R_b(Tb/s)	L_{bit}(μm)	SD(b/μm)
TE	0.90	0.525	0.0103	0.2361	365.99	67.7	14.50	0.6331	48.33	2.1128	4.90	0.2042
	0.90	0.55	0.0115	0.2405	372.8	74.1	14.35	0.6858	47.83	2.3125	4.52	0.2212
	0.90	0.575	0.011	0.2431	376.85	70.2	14.46	0.6545	48.20	2.1900	4.74	0.2111
	0.90	0.60	0.0109	0.2469	382.65	68.5	14.52	0.6421	48.40	2.1398	4.83	0.2071
	0.95	0.525	0.0103	0.2383	369.39	67.3	14.11	0.6127	47.03	2.1012	5.06	0.1977
	0.95	0.55	0.0098	0.242	375.11	62.6	14.36	0.5799	47.87	1.9542	5.35	0.1871
	0.95	0.575	0.0096	0.2449	379.59	60.9	14.65	0.5752	48.83	1.8997	5.39	0.1855
	0.95	0.60	0.0096	0.2484	384.96	59.7	15.364	0.5916	51.21	1.8630	5.24	0.1908
TM	0.85	0.65	0.0038	0.2958	458.45	19.7	37.72	0.4788	125.7	0.6142	6.47	0.1545
	0.85	0.675	0.0034	0.3023	468.56	17.4	39.92	0.4469	133.1	0.5417	6.94	0.1442
	0.85	0.70	0.0033	0.3108	481.75	16.7	41.74	0.4494	139.1	0.5209	6.90	0.145
	0.90	0.65	0.0049	0.2983	462.32	25.6	30.96	0.5122	103.2	0.8005	6.05	0.1652
	0.90	0.675	0.0045	0.3048	472.48	22.9	32.257	0.4771	107.5	0.7157	6.50	0.1539
	0.90	0.70	0.0044	0.3134	485.73	21.9	33.97	0.4799	113.2	0.6836	6.46	0.1548

highest compatible value of $NDBP = 0.5122$ for the operating bandwidth of 25.6425 nm and group index 30.96. The longest storage time is achieved in this case but in the account of bandwidth. At the optimum for TM mode, R_b is 0.8005 Tb/s with the small physical size of each stored bit around 6.0525 μm, corresponding to $SD = 0.1652$ bit/μm. As the present optical modulators [28], [29] has the modulation speed of $10 - 100$ Gb/s, the proposed SSPCW can be utilized for developing high-speed optical modulator. Besides, SD of slow light in practical PhC delay line devices is 1 bit/20 μm [30]. Whereas our SD for TE SSPCW is 0.2212 bit/μm, and 0.1652 bit/μm for TM SSPCW. Finally, to obtain further optimum results for TM mode, we consider-changing the displacement between each adjacent slots form $s_z = 0.06a$ to $0.1a$ by an increment of $\Delta s_z = 0.01a$, while keeping $w_x = 0.90a$ and $l_z = 0.65a$ at the optimum values as shown in Table 2. The influence of s_z on n_g is shown in Fig. 5 and Table 3. It is comprehended from Table 3 that for $s_z = 0.07a$, it has an $\overline{n}_g$ of 9.73, and there are the largest R_b and wider bandwidth $\Delta\lambda$ about 1.9142 Tb/s and 61.3192 nm respectively, with the lowest 1-bit storage size of 8.0534 μm. Therefore, ultra-high R_b was achieved for both TE and TM modes. This is significant as in future telecommunication networks, high R_b, all-optical signal processing exceeding 40 Gb/s will be desirable [31] and 1 Tb/s for metro transportation systems [32]. Also, the SSPCW can provide promising applications for random access memories in all-optical signal processors and quantum information processing.

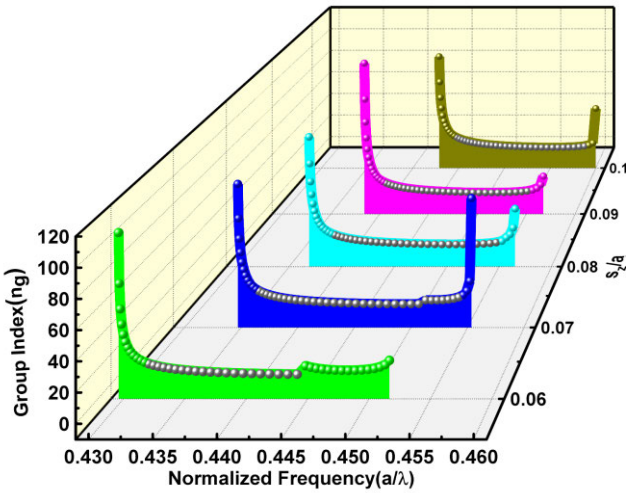

FIGURE 5. n_g versus normalized frequency a/λ for TM modes with varying s_z from $0.06a$ to $0.1a$ at $w_x = 0.90a$ and $l_z = 0.65a$.

IV. TIME-DOMAIN ANALYSES

To validate our results founded by PWE method, the time-domain propagation of optical pulse is studied over the proposed SSPCW with the two-dimensional finite-difference time-domain (2D-FDTD) method through FullWAVE module of software Rsoft [33] with 25 grid points in resolution for each period and perfectly matched absorbing boundary layers (PMLs) surrounding the structure. The transmission length is elongated to be $50a$. $\overline{n}_g$ is calculated from [26] $\overline{n}_g = c\Delta T/L$, where ΔT is delay time by ps unit between the input and output pulses and L is transmission length. Throughout the simulation, two monitors are positioned to measure the field intensity. To grantee being inside the slow-light region, the input monitor is located inside at a position of $10a$ to the leftmost air-hole row and the output monitor is located at a position of $10a$ to the rightmost air-hole row of the structure, so the transmission length monitored is $L = 30a$.

Three cases are considered for 2D-FDTD simulations. The first case is the optimized instance for TE mode at $w_x = 0.90a$, $l_z = 0.55a$ and $s_z = 0.0a$ with $\overline{n}_g = 14.35$ and $\Delta\lambda = 74.0776$ nm at 1550 nm. According to Table 2 and clear comparison between PWE and FDTD methods, the Gaussian pulse source is launched with central normalized frequency $U_0 = 0.2405$ and to operate at optical communication wavelength of 1550 nm, the lattice constant a is 372 nm. Fig. 6(a) reveals the intensity of the normalized field of input and output monitors with the time delay by ps. As clarified, the normalized field intensities detected by the input and output monitors are at 2.384 ps and 2.873 ps respectively, thus the delay time ΔT between the input and output is 0.489 ps over the length $L = 30a$. Consequently, $\overline{n}_g = 13.11$. The slight difference between the two values of $\overline{n}_g$ from PWE and FDTD is principally

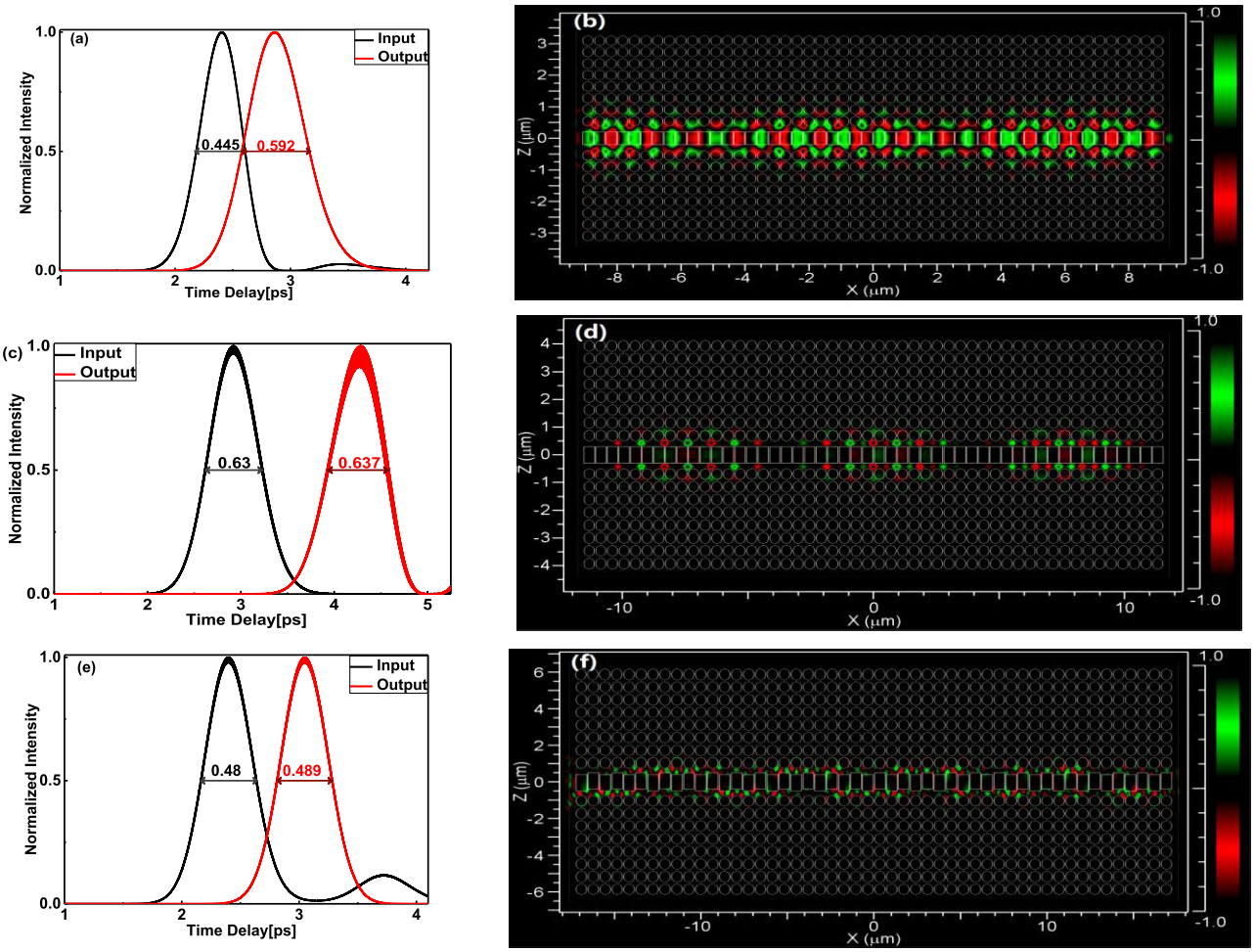

FIGURE 6. (a) Time-domain optical-pulse transmission in the optimized TE SSPCW with $w_x = 0.90a$, $l_z = 0.55a$ and $s_z = 0.0a$, with (b) the E-field distribution inside the SSPCW; (c) time-domain optical-pulse transmission in the TM SSPCW with $w_x = 0.90a$, $l_z = 0.65a$ and $s_z = 0.0a$, with (d) the M-filed profile; (e) time-domain optical-pulse transmission in the TM SSPCW with $w_x = 0.90a$, $l_z = 0.65a$ and $s_z = 0.07a$, with (f) the M-filed profile.

from the number of plane waves for calculation in the PWE method and the limited discretization of FDTD [34]. The full widths at half maximum (FWHM) detected by the input and output monitors are 0.445 ps and 0.592 ps, respectively, viewing a pulse distortion. This displays that the relative pulse distortion ($D_p = FWHM_{out}/FWHM_{in} - 1$) is 33.0337% and the relative pulse distortion per unit length ($D_{PR} = D_P/L$) is 2.9536 % μm^{-1}, which is a little high. The light pulse transmission for TE inside the designed SSPCW has a benefit to realizing the physical mechanism as shown in Fig. 6(b). The Electric field (E-field) profile shows that the pulse transmission is slow and completely different from the counterpart in conventional PCWs. The E- field profile reflects a wider bandwidth. The second case is the optimized instance for TM mode at $w_x = 0.90a$, $l_z = 0.65a$ and $s_z = 0.0a$ with $\overline{n}_g = 30.96$ and $\Delta\lambda = 25.6425$ nm at 1550 nm. According to Table 2, the Gaussian pulse source is launched with $U_0 = 0.2983$ and $a = 462$ nm. From Fig. 6(c), the normalized field intensities detected by the input and output monitors are at 4.298 ps and 2.912 ps respectively, thus ΔT between the input and output is 1.386 ps over the length $L = 30a$. Consequently, $\overline{n}_g = 30$. The FWHMs detected by the input and output monitors are 0.630 ps and 0.637 ps respectively, viewing a very small pulse distortion of $D_p = 1.1111\%$ and $D_{PR} = 0.0801$ % μm^{-1}. The magnetic field (M-field) profile of pulse transmission is shown in Fig. 6(d), which reflects a lower transmission bandwidth as compared with that of TE mode transmission in Fig. 6(b). Periodic oscillations of the field profile are observed through spatial light confinement along the propagation path. It displays that the pulse experiences periodic compression, extension, and compression, and the output of the pulse width is nearly the same as that of the input pulse. The third case is the optimized instance for TM mode at $w_x = 0.90a$, $l_z = 0.65a$ and $s_z = 0.07a$ with $\overline{n}_g = 9.73$ and $\Delta\lambda = 61.3192$ nm at 1550 nm. According to Table 3, the Gaussian pulse source is launched with $U_0 = 0.4454$ and $a = 690$ nm. From Fig. 6(e), the normalized field intensities detected by the input and output monitors are at 2.387 ps and 3.058 ps respectively, thus ΔT between input and output pulses is 0.671 ps over $L = 30a$.

TABLE 3. Slow-light and all-optical buffer parameters for TM modes at $w_x = 0.90a$, $l_z = 0.65a$ and different s_z values.

s_z/a	ΔU	U_0	a(nm)	$\Delta\lambda$ at 1550 nm	$\overline{n}_g$	$NDBP$	T_s(ps)	R_b(Tb/s)	L_{bit}(μm)	SD(b/μm)
0.06	0.0121	0.43813	679.1	42.67	8.74	0.2406	29.13	1.332	12.88	0.0776
0.07	0.0176	0.44541	690.3	61.319	9.73	0.3849	32.43	1.914	8.05	0.1242
0.08	0.0154	0.44704	692.9	53.32	9.22	0.3172	30.73	1.664	9.77	0.1023
0.09	0.0145	0.44787	694.2	50.	9.8	0.3162	32.67	1.561	9.8	0.102
0.10	0.014	0.45174	700.2	47.97	10.62	0.3286	35.4	1.497	9.43	0.106

TABLE 4. Comparison between current work and previous literature.

Refs.	Polarization	GVD order	$NDBP$	L_{bit}(μm)
Current work	TE	10^4	0.6858	4.52
	TM	10^5	0.5122	6.05
[11]	TE only	10^6	0.14	Non
[12]	TE only	10^6	0.221	Non
[13]	TE only	10^6	0.31	Non
[17]	TE only	10^5	0.4661	6.95
[35]	TE only	10^8	0.245	Non

TABLE 5. GVD within ±7.5% variation of n_g and distortion of the optimum SSPCW for TE/TM operations.

Mode	w_x/a	l_z/a	s_z/a	GVD with in ±7.5 %	$FWHM_{in}$(ps)	$FWHM_{out}$(ps)	D_{PR}(%/μm)
TE	0.90	0.55	0.00	-9.021×10^3 to 2.353×10^3	0.445	0.592	2.95
TM	0.90	0.65	0.00	-3.744×10^4 to 1.560×10^4	0.630	0.637	0.08
TM	0.90	0.65	0.07	-4.680×10^3 to 3.404×10^3	0.480	0.489	0.09

Consequently, $\overline{n}_g = 9.725$ which agrees completely with the PWE calculations. The FWHMs for the input and output monitors are 0.48 ps and 0.489 ps respectively, viewing also a very small pulse distortion of $D_p = 1.8750\%$ and $D_{PR} = 0.0905\ \%\ \mu\text{m}^{-1}$. Thus, the pulses can be transmitted lengthways in the proposed SSPCW without explicit distortion. The magnetic field profile of pulse transmission is shown in Fig. 6(f), which shows that the distortion in the pulse transmission is ignorable. The proposed SSPCW provides an abundant higher value of slow-light property ($NDBP$) and all-optical buffer parameters compared with all other structures based on slotted PCW waveguides reported previously in literature as shown in Table 4. In comparison with previous works, we find that our work has achieved high $NDBPs$ in the cases of both TE and TM. Ultra-low dispersion is achieved within ±7.5% of the group index in the proposed SSPCW, unlike previous literature that achieved results with a change in ±10% of the group's index.

V. IMPLEMENTATION CONSIDERATIONS

There are a few particular issues for the implementation of buffer devices, for instance, dispersion, losses and fabrication tolerance, to be considered.

A. GVD

The second derivative of dispersion relation gives the group velocity dispersion ($GVD = d^2k/d\omega^2 = (a/2\pi c^2)dn_g/dU$) which induces phase modulation and results in pulse width broadening. Subsequently, the carried bit data by the transmitted pulses become distorted along the propagation path. Therefore, compensation to the distortion due to the GVD along the propagation is required [1], [6], [36]. Naturally, less distortion (L-D) corresponds to less GVD (L-GVD) in transmission. So, we searched for low dispersion distortion (L-DD). Fig. 7 shows the GVD variation of optimum cases for TE/TM SSPCWs within ±7.5 % variation of n_g color in green. The ±7.5 % variation of n_g is a small variation for the light to have ultra-low dispersion, i.e., nearly zero dispersion. To see the masked range of green color in the GVD curve clearly, the corresponding data in Fig. 7 is transferred into Table 5 with a summary of distortion calculation in the previous section for the optimum cases.

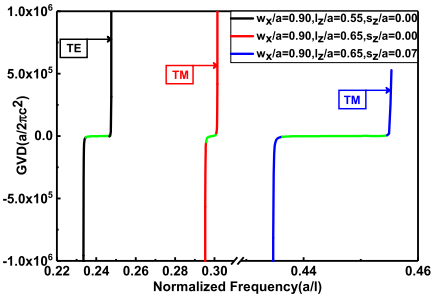

FIGURE 7. GVD variation with normalized frequency a/λ of the SSPCW within the ±7.5% variation of n_g colored in green for optimum cases.

As shown in Table 5, ultra-low dispersion is achieved within the ±7.5% of the group index. For general application, we can consider $GVD < 10^6(a/2\pi c^2)$ as low GVD, and then all our proposed SSPCWs are ultra L-DD and they are proper for optical pulse transmission and all-optical buffer applications [37]. As can be seen from Table 5, within the ±7.5% variation of group index, it is sufficient to achieve ultra-low

dispersion below $1 \times 10^4(a/2\pi c^2)$ and $1 \times 10^5(a/2\pi c^2)$ of GVD for TE and TM modes, respectively. Alternatively, an appropriate GVD can be used to compensate for the pulse distortion. For compensation purposes, the designs having positive and negative GVDs are shown in Fig. 7. Besides, slow light transmitted in a waveguide experience generally an intrinsic dispersion. Hence, designing a wide zero-dispersion band is required for slow-light systems and important for high fidelity in the transmission of light signals.

B. LOSSES

In general, there are two classes of losses: material loss and structure loss. By using appropriate materials, material loss can be neglected or avoided [2], [38]. Structure loss for PCWs or any waveguide possesses two originations. The first one is the coupling loss at the input and output of a structure or a device; the second one is the propagation loss through the buffer region. To conserve the bandwidth and storage advantages of buffer devices, it is adequate to employ classical Si waveguide as a transmission medium devoid of any loss, and use a buffer and slow-light devices as active elements [39]. Now, coupling loss in the buffer and slow-light devices can be considered as a mostly resolved issue [4], [39], [40]. Propagation losses in the slow light and buffer PCW can be classified into intrinsic and extrinsic losses. For the practical realization of slow-light devices, the dispersion curve of waveguide modes should be under the light line, because the modes located above the light line are extremely lossy, and the modes below the light line are intrinsically lossless [26] and all our calculations are done below light lines. Providentially, both issues of the dispersion and losses are controlled by particular designs of the proposed structures since the benefited property of the slow light is a joint result by the pulse broadening and loss [4], [41]. So, the design of compensating-device GVD with opposite signs shown in Fig. 7 is proposed for overcoming the pulse broadening. For the issue of propagation losses, the optimized case of TE SSPCW is considered for a transmission length $L = 50a$ with $w_x = 0.90a$, $l_z = 0.55a$, $s_z = 0.0a$, and $a = 373$ nm. A Gaussian pulse source is launched by using 2-D FDTD method with 4 monitors inserted every $10a$ where the first monitor is positioned at $10a$ from the leftmost row of the SSPCW for observing the attenuation in the slow-light region, and the last monitor is located at $10a$ from the rightmost row of the SSPCW. Hence, the distance is $L = 30a$ between the first and last monitors.

Fig. 8 shows the contour map of transmitted power versus central operating wavelength and delay time at 4 different monitors for the optimized TE SSPCW. The 4 monitors are arranged every $10a$ inside the slow-light region. From Fig. 8, the transmission band is observed over the full c-band that reflects the wide transmission bandwidth along the propagation path and confirmed our proposed results by the PWE method. The magnitudes of optical pulse power at the first to fourth monitors are 0.746 a.u., 0.734 a.u.,

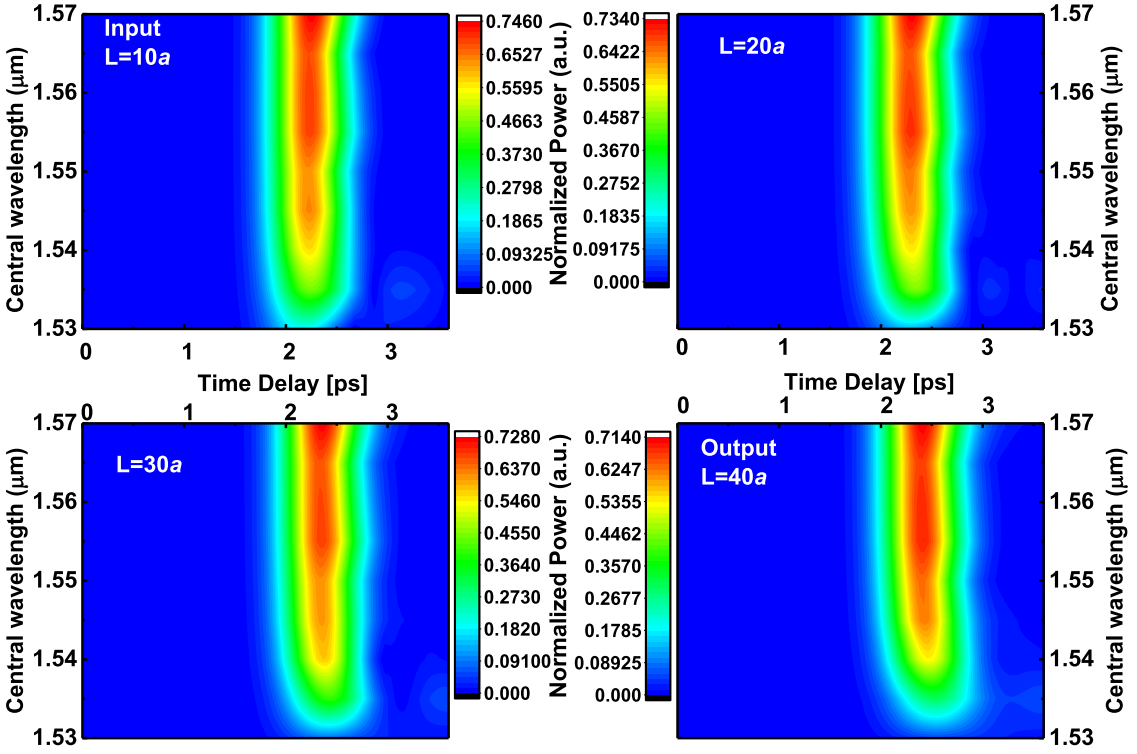

FIGURE 8. Contour map of transmitted power versus central operating wavelength and delay time at 4 different monitors for the optimized TE SSPCW of $w_x = 0.90a$, $l_z = 0.55a$, $s_z = 0.0a$, and a = 373 nm. The 4 monitors are arranged every $10a$ inside the slow-light region.

0.728 a.u. and 0.714 a.u., respectively, showing a decay along the transmission path. The attenuation coefficient is 0.0189 dB/μm between the first and second monitors ($L = 10a$ and $a = 0.373$ μm), 0.0095 dB/μm between the second and third monitors, and 0.0226 dB/μm between the third and fourth monitors. Thus, The average attenuation coefficient of 0.0170 dB/μm, is a lower attenuation (L-A) compared to that reported in the literature [42]–[44]. For example, in [42], the attenuation was 1.5 dB/μm and in [43] was 0.05 dB/μm. However, less attenuation is better for applications, and thus it is an interesting future work to acquire further less attenuation. Moreover, we achieved low DDA in one proposed structure and further, we will show that this structure is insensitive for a small variation of structure parameters, which represents a challenge in the fabrication of conventional PCWs.

C. FABRICATION TOLERANCE

After designing any proposed structure, the fabrication of buffer devices on a large scale is one of the critical issues. Attributable to the inadequate process of equipment in the progression of fabrication, there may exist rough changes between the simulated results and that of the structure fabricated. The errors include, for example, that due to the electron scattering in electron beam lithography, etching anisotropies, and stitching [45]. These errors lead to the changing of air holes in the basic PhC and also the slot width and length in the structure. As the PBG is larger than the bandwidth of the transmitted slow-light pulse, thus the errors of air holes involving the PhC structure can be neglected. Consequently, acceptable tolerance of the slot width and length is modeled by changing w_x and l_z around the optimum values of $0.90a$ and $0.55a$ respectively for TE SSPCW. Table 6 displays 9 cases of fabrication errors of the optimized TE SSPCW. The width w_x changes from $0.54a$ to $0.56a$ around the optimized value $0.55a$ by $\pm 0.01a = \pm 3.73$ nm at $a = 373$ nm. The length l_z changes from $0.89a$ to $0.91a$ around the optimized value $0.90a$ by $\pm 0.01a = \pm 3.73$ nm. The results in Table 6 show that $\overline{n}_g$ is scrimpy ranging from 14.23 to 14.51 over a narrow changing of bandwidth from 70.2515 nm to 74.9807 nm, with average values exposed in the last line. The averaged R_b, L_{bit} and SD of 2.2803 Tb/s, 4.58 μm and 0.2184 b/μm respectively are significantly close to the optimum values in No. 5. Moreover, the slow-light and all-optical buffer parameters have insignificant variation. Hence, the errors are totally acceptable in this range and thus the deviation is virtually negligible about the optimum values. Finally, we can conclude that below the variation of $\pm 0.01a$ around ± 3 *nm* there is no deviation between the simulated results and that of fabricated structure. So, the proposed PCW with sporadic slots in the waveguide is insensitive for small variations of waveguide parameters, which is the challenge in conventional PCW fabrication.

TABLE 6. The effect of fabrication tolerance on slow-light and all-optical buffer parameters.

No.	w_x /a	l_z /a	$\Delta\lambda$	$\overline{n}_g$	R_b(Tb /s)	L_{bit}(μm)	SD(b /μm)
1	0.89	0.54	70.25	14.38	2.193	4.76	0.2102
2	0.89	0.55	74.89	14.23	2.338	4.51	0.2218
3	0.89	0.56	74.43	14.25	2.323	4.53	0.2207
4	0.90	0.54	72.39	14.37	2.26	4.62	0.2165
5	0.90	0.55	74.08	14.34	2.313	4.52	0.2211
6	0.90	0.56	73.57	14.37	2.297	4.54	0.2200
7	0.91	0.54	74.22	14.41	2.317	4.49	0.2226
8	0.91	0.55	73.23	14.46	2.286	4.54	0.2204
9	0.91	0.56	70.34	14.51	2.196	4.71	0.2124
AVG.	/	/	73.04	14.36	2.28	4.58	0.2184

VI. CONCLUSION

In conclusion, a new paradigm structure (SSPCW) is inspected based on the SPCW. The results are numerically discussed for all-optical buffers and slow-light property of TE and TM polarized modes by PWE and confirmed with FDTD methods for the first time. Besides, low DDA is obtained. By appropriately modifying the sporadic-slot dimensions, higher buffer performance and wider transmission bandwidth in the telecommunication band are demonstrated. The bandwidth centered at 1550 *nm* fluctuates from 16.7 *nm* to 75 *nm*, corresponding to a fluctuation of the bit rate from 0.5209 *Tb/s to* 2.3125 *Tb/s* within $\pm 7.5\%$ variation of group index which is a sufficient guarantor to achieve ultra-low dispersion below $5 \times 10^4 (a/2\pi c^2)$ with the highest value of NDBP about 0.6858 and 0.5122 for TE and TM modes, respectively. For low distortion, the incident optical pulse of width 0.63 ps is broadened to be solitary 0.637 ps, corresponding to a relative pulse distortion along the propagation path per unit length of 0.0801 % μm^{-1}. Moreover, the attenuation coefficient of the optical-pulse power between the input and output is obtained as 0.0170 $dB/\mu m$.

REFERENCES

[1] J. Li, T. P. White, L. O'Faolain, A. Gomez-Iglesias, and T. F. Krauss, "Systematic design of flat band slow light in photonic crystal waveguides," *Opt. Express*, vol. 16, no. 9, pp. 6227–6232, Apr. 2008.

[2] S. Yan, Z. Cheng, L. H. Frandsen, Y. Ding, F. Zhou, J. Dong, and X. Zhang, "Bandwidth-adaptable silicon photonic differentiator employing a slow light effect," *Opt. Lett.*, vol. 42, no. 8, pp. 1596–1599, Apr. 2017.

[3] M. Danaie, A. Geravand, and S. Mohammadi, "Photonic crystal double-coupled cavity waveguides and their application in design of slow-light delay lines," *Photon. Nanostruct.-Fundam. Appl.*, vol. 28, pp. 61–69, Feb. 2018.

[4] S. Elshahat, I. Abood, K. Khan, A. Yadav, L. Bibbo, and Z. Ouyang, "Five-line photonic crystal waveguide for optical buffering and data interconnection of picosecond pulse," *J. Lightw. Technol.*, vol. 37, no. 3, pp. 788–798, Feb. 1, 2019.

[5] J. D. Ryckman and S. M. Weiss, "Localized field enhancements in guided and defect modes of a periodic slot waveguide," *IEEE Photon. J.*, vol. 3, no. 6, pp. 986–995, Dec. 2011.

[6] T. F. Krauss, "Slow light in photonic crystal waveguides," *J. Phys. D, Appl. Phys.*, vol. 40, no. 9, pp. 2666–2670, 2007.

[7] C.-Y. Lin, A. X. Wang, W.-C. Lai, J. L. Covey, S. Chakravarty, and R. T. Chen, "Coupling loss minimization of slow light slotted photonic crystal waveguides using mode matching with continuous group index perturbation," *Opt. Lett.*, vol. 37, no. 2, pp. 232–234, Jan. 2012.

[8] W.-C. Lai, S. Chakravarty, X. Wang, C. Lin, and R. T. Chen, "Photonic crystal slot waveguide absorption spectrometer for on-chip near-infrared spectroscopy of xylene in water," *Appl. Phys. Lett.*, vol. 98, no. 2, Jan. 2011, Art. no. 023304.

[9] P. Xu, J. Zheng, J. Zhou, Y. Chen, C. Zou, and A. Majumdar, "Multi-slot photonic crystal cavities for high-sensitivity refractive index sensing," *Opt. Express*, vol. 27, no. 3, pp. 3609–3616, Feb. 2019.

[10] J. Jágerská, H. Zhang, Z. Diao, N. L. Thomas, and R. Houdré, "Refractive index sensing with an air-slot photonic crystal nanocavity," *Opt. Lett.*, vol. 35, no. 15, pp. 2523–2525, Aug. 2010.

[11] Y. Zhao, Y.-N. Zhang, and H.-F. Hu, "Dispersion engineering of slow light in ellipse-shaped-hole slotted photonic crystal waveguide," *J. Lightw. Technol.*, vol. 32, no. 11, pp. 2144–2151, Jun. , 2014.

[12] S. Serna, P. Colman, W. Zhang, X. Le Roux, C. Caer, L. Vivien, and E. Cassan, "Experimental GVD engineering in slow light slot photonic crystal waveguides," *Sci. Rep.*, vol. 6, no. 1, Jul. 2016, Art. no. 26956.

[13] H. Aghababaeian, M.-H. Vadjed-Samiei, and N. Granpayeh, "Temperature stabilization of group index in silicon slotted photonic crystal waveguides," *J. Opt. Soc. Korea*, vol. 15, no. 4, pp. 398–402, Dec. 2011.

[14] Y. Zhao, Y.-N. Zhang, D. Wu, and Q. Wang, "Wideband slow light with large group index and low dispersion in slotted photonic crystal waveguide," *J. Lightw. Technol.*, vol. 30, no. 17, pp. 2812–2817, Sep. 1, 2012.

[15] A. Di Falco, L. O'Faolain, and T. F. Krauss, "Dispersion control and slow light in slotted photonic crystal waveguides," *Appl. Phys. Lett.*, vol. 92, no. 8, Feb. 2008, Art. no. 083501.

[16] C. Caer, X. Le Roux, V. K. Do, D. Marris-Morini, N. Izard, L. Vivien, D. Gao, and E. Cassan, "Dispersion engineering of wide slot photonic crystal waveguides by Bragg-like corrugation of the slot," *IEEE Photon. Technol. Lett.*, vol. 23, no. 18, pp. 1298–1300, Sep. 15, 2011.

[17] Y. Zhai, H. Tian, and Y. Ji, "Slow light property improvement and optical buffer capability in ring-shape-hole photonic crystal waveguide," *J. Lightw. Technol.*, vol. 29, no. 20, pp. 3083–3090, Oct. 15, 2011.

[18] Y. Wan, K. Fu, C. Li, and M. Yun, "Improving slow light effect in photonic crystal line defect waveguide by using eye-shaped scatterers," *Opt. Commun.*, vol. 286, pp. 192–196, Jan. 2013.

[19] B. Meng, L.-L. Wang, X.-F. Li, W.-Z. Xiao, L. Wang, and D. Xiang, "Novel slow-light waveguide with large bandwidth and ultra low dispersion," *Opt. Commun.*, vol. 285, no. 18, pp. 3704–3708, Aug. 2012.

[20] L. H. Frandsen, A. V. Lavrinenko, J. Fage-Pedersen, and P. I. Borel, "Photonic crystal waveguides with semi-slow light and tailored dispersion properties," *Opt. Express*, vol. 14, no. 20, pp. 9444–9450, Oct. 2006.

[21] F. Long, H. Tian, and Y. Ji, "A study of dynamic modulation and buffer capability in low dispersion photonic crystal waveguides," *J. Lightw. Technol.*, vol. 28, no. 8, pp. 1139–1143, Apr. 15, 2010.

[22] S. Elshahat, I. Abood, K. Khan, A. Yadav, and Z. Ouyang, "High-capability micro-optical buffer based on coupled hexagonal cavity in photonic crystal waveguide," *Appl. Nanosci.*, vol. 9, no. 8, pp. 1963–1970, Nov. 2019.

[23] R. S. Tucker, P.-C. Ku, and C. J. Chang-Hasnain, "Slow-light optical buffers: Capabilities and fundamental limitations," *J. Lightw. Technol.*, vol. 23, no. 12, pp. 4046–4066, Dec. 2005.

[24] Q. Quan, P. B. Deotare, and M. Loncar, "Photonic crystal nanobeam cavity strongly coupled to the feeding waveguide," *Appl. Phys. Lett.*, vol. 96, no. 20, May 2010, Art. no. 203102.

[25] I. Abood, S. Elshahat, K. Khan, L. Bibbò, A. Yadav, and Z. Ouyang, "Slow light with high normalized delay-bandwidth product in low-dispersion photonic-crystal coupled-cavity waveguide," *Opt. Commun.*, vol. 439, pp. 181–186, May 2019.

[26] S. Elshahat, I. Abood, K. Khan, A. Yadav, Q. Wang, Q. Liu, M. Lin, K. Tao, and Z. Ouyang, "Ultra-wideband slow light transmission with high normalized delay bandwidth product in W3 photonic crystal waveguide," *Superlattices Microstruct.*, vol. 121, pp. 45–54, Sep. 2018.

[27] S. Elshahat, I. Abood, K. Khan, A. Yadav, L. Bibbò, and Z. Ouyang, "Ultra-high group index slow light with optical buffering performance in photonic crystal waveguide coupled with cavity," *Proc. SPIE*, vol. 10825, Nov. 2018, Art. no. 1082513.

[28] H. C. Nguyen, Y. Sakai, M. Shinkawa, N. Ishikura, and T. Baba, "10 Gb/s operation of photonic crystal silicon optical modulators," *Opt. Express*, vol. 19, no. 14, pp. 13000–13007, Jul. 2011.

[29] W. M. Green, M. J. Rooks, L. Sekaric, and Y. A. Vlasov, "Ultra-compact, low RF power, 10 Gb/s silicon mach-zehnder modulator," *Opt. Express*, vol. 15, no. 25, pp. 17106–17113, 2007.

[30] R. S. Tucker, "Capabilities and limitations of slow light optical buffers: Searching for the killer application," in *Proc. Conf. Lasers Electro-Opt./Int. Quantum Electron. Conf.*, 2009, p. 1.

[31] C. Monat, B. Corcoran, D. Pudo, M. Ebnali-Heidari, C. Grillet, M. D. Pelusi, D. J. Moss, B. J. Eggleton, T. P. White, L. O'Faolain, and T. F. Krauss, "Slow light enhanced nonlinear optics in silicon photonic crystal waveguides," *IEEE J. Sel. Topics Quantum Electron.*, vol. 16, no. 1, pp. 344–356, Feb. 2010.

[32] S. E. Alavi, M. R. K. Soltanian, I. S. Amiri, M. Khalily, A. S. M. Supa'at, and H. Ahmad, "Towards 5G: A photonic based millimeter wave signal generation for applying in 5G access fronthaul," *Sci. Rep.*, vol. 6, no. 1, Apr. 2016, Art. no. 19891.

[33] S. Rahimi, A. Hosseini, X. Xu, H. Subbaraman, and R. T. Chen, "Group-index independent coupling to band engineered SOI photonic crystal waveguide with large slow-down factor," *Opt. Express*, vol. 19, no. 22, pp. 21832–21841, Oct. 2011.

[34] K. Üstün and H. Kurt, "Ultra slow light achievement in photonic crystals by merging coupled cavities with waveguides," *Opt. Express*, vol. 18, no. 20, p. 21155–21161, Sep. 2010.

[35] N. Zhu, Y. Li, C. Chen, and S. Yan, "Slow light in dual-periodic photonic crystals based slotted-waveguide coupled cavity," *Opt. Laser Technol.*, vol. 83, pp. 125–130, Sep. 2016.

[36] A. Y. Petrov and M. Eich, "Zero dispersion at small group velocities in photonic crystal waveguides," *Appl. Phys. Lett.*, vol. 85, no. 21, pp. 4866–4868, Nov. 2004.

[37] J. Tang, T. Wang, X. Li, B. Liu, B. Wang, and Y. He, "Systematic design of wideband slow light in ellipse-hole photonic crystal waveguides," *J. Opt. Soc. Amer. B, Opt. Phys.*, vol. 31, no. 5, pp. 1011–1017, May 2014.

[38] E. D. Palik, Ed., "Preface," in *Handbook of Optical Constants of Solids*. Burlington, MA, USA: Academic, 1997.

[39] H. S. Dutta, A. K. Goyal, V. Srivastava, and S. Pal, "Coupling light in photonic crystal waveguides: A review," *Photon. Nanostruct.-Fundam. Appl.*, vol. 20, pp. 41–58, Jul. 2016.

[40] M. Hosseinpour, M. Ebnali-Heidari, M. Kamali, and H. Emami, "Optofluidic photonic crystal slow light coupler," *J. Opt. Soc. Amer. B, Opt. Phys.*, vol. 30, no. 3, pp. 717–722, Mar. 2013.

[41] Y. A. Vlasov, M. O'Boyle, H. F. Hamann, and S. J. McNab, "Active control of slow light on a chip with photonic crystal waveguides," *Nature*, vol. 438, no. 7064, pp. 65–69, Nov. 2005.

[42] K. Abedi and S. M. Mirjalili, "Slow light performance enhancement of Bragg slot photonic crystal waveguide with particle swarm optimization algorithm," *Opt. Commun.*, vol. 339, pp. 7–13, Mar. 2015.

[43] S. M. Mirjalili, "Ellipse-ring-shaped-hole photonic crystal waveguide," *Optik*, vol. 126, no. 1, pp. 56–60, 2015.

[44] R. Hao, X.-L. Peng, E.-P. Li, Y. Xu, J.-M. Jin, X.-M. Zhang, and H.-S. Chen, "Improved slow light capacity in graphene-based waveguide," *Sci. Rep.*, vol. 5, no. 1, Dec. 2015, Art. no. 15335.

[45] M. Y. Tekeste and J. M. Yarrison-Rice, "High efficiency photonic crystal based wavelength demultiplexer," *Opt. Express*, vol. 14, no. 17, pp. 7931–7942, Aug. 2006.

SAYED ELSHAHAT received the B.Sc. and M.Sc. degrees from Assuit University, Assuit, Egypt, in 2008 and 2014, respectively, and the Ph.D. degree from Shenzhen University, China, in 2019. He currently holds a postdoctoral position at the Institute of Microscale Optoelectronics, Shenzhen University. His research interest includes the compression of ultrashort light pulses and slow light process in photonic crystals.

ISRAA ABOOD received the B.Sc. and M.Sc. degrees from Assuit University, Assuit, Egypt, in 2008 and 2017, respectively. She is currently pursuing the Ph.D. degree with the Key Laboratory of Optoelectronics Devices and Systems, Ministry of Education and Guangdong Province, Shenzhen University, Shenzhen, China. Her research interests include Fano resonance in photonic crystals and optical communication.

ZIXIAN LIANG received the Ph.D. degree from the Chinese Academy of Sciences, in 2010. He is currently an Associate Professor with the Institute of Microscale Optoelectronics, Shenzhen University. His research interests primarily include photonics crystals, metamaterials, and transformation optics.

JIHONG PEI (Member, IEEE) was born in Gansu, China. He received the Ph.D. degree from the Xi'an University of Electronic Science and Technology, in 1998. From 1989 to 2002, he worked at the Xi'an University of Electronic Science and Technology. He has been with Shenzhen University, since 2002, where he is currently the Director of the Department of Electronics, School of Information Engineering, and also works with the ATR National Defense Science and Technology Key Laboratory. His main research interests include image and video content analysis, intelligent video surveillance, multicamera panoramic video technology, pattern recognition and machine learning, multispectral remote sensing image analysis, vector field signals, and image analysis. He is a member of the China Aeronautical Member Information Fusion Branch.

ZHENGBIAO OUYANG (Member, IEEE) received the B.S. degree in radio engineering from the Harbin Institute of Technology, Harbin, China, in 1983, and the Ph.D. degree in electron physics from the University of Electronic Science and Technology of China, in 1988. He is currently a Full Professor and the Director of the Solid-State Photonics Laboratory, Shenzhen University, the Vice Director of the THz Technical Research Center, Shenzhen University, the Vice Director of the Shenzhen Key Laboratory of Micro–Nano Photonic Information Technology, a Trustee of the Chinese Society of Optical Engineering, a Committeeman of the Opto-Electronic Committee of the Chinese Space Aeronautics Association, a Senior Member of the Chinese Optical Society, and a member of the Optical Society of America. His main research interests in recent years include nano photonic materials, optical logic integrated circuits, nano photonic devices based on photonic crystals, metamaterials, and metasurfaces, high-speed optical communication technology, and THz technology.